

Research Project in Magnetism

Sky-MoCa

The Skyrmion Phase in 3D Lattice Simulations



by

Niki Kilbertus

supervised by

Prof. Dr. Christian Back

Faculty for Physics
University of Regensburg

October 2016

Abstract

We use the three-dimensional spin lattice Monte Carlo code *Sky-MoCa* to investigate the skyrmion phase in chiral magnets non-perturbatively. We derive the appropriate lattice Hamiltonian and discuss the relevant interactions as well as their consequences. The thermodynamic phases and transitions between them can be analyzed by means of Bragg intensity patterns and thermodynamic properties such as the specific heat and the susceptibility. We specifically demonstrate that the model does indeed exhibit the helical, conical and skyrmion phase for appropriate choices of the temperature and the external field. Subsequently we study the temperature driven transition from the unordered random phase to the helical phase. Moreover, we cool the system into the skyrmion phase and simulate both transitions driven by a change of the magnetic field. First, we decrease the field until the skyrmion tubes start to touch and gradually merge eventually resulting in the helical phase. Secondly, we increase the magnetic field until the skyrmion tubes simply vanish and the system transitions into the fully aligned phase. All observed phenomena qualitatively match experimental data.

Contents

1	Theoretical background	1
1.1	Introduction	1
1.2	The Spin Lattice Model	2
1.3	Interactions	4
1.4	The Hamiltonian	6
1.5	Observables and Analysis	9
2	Results	13
2.1	Thermodynamic Phases	13
2.2	The Helimagnetic Phase Transition	15
2.3	Unwinding Skyrmions	16
2.4	Conclusion	19
	References	21

1 Theoretical background

1.1 Introduction

Many crystals with a lack of inversion symmetry show an interesting phase consisting of a regular arrangement of magnetic whirl tubes called skyrmions. These spin configurations are found in a wide range of chiral magnets [11, 12, 15, 23, 22, 17, 10, 20, 13, 16] and have received a lot of attention lately mostly due to the topological stability of a quantized winding number associated with the whirl tubes. Defect mobility or skyrmion switching [7] might make them suitable candidates for a permanent fast and efficient memory or other spintronic devices.

Besides direct observation through a variety of experimental techniques, numeric simulations have contributed significantly to the understanding of skyrmions [6, 10, 7]. The typical setup is a three-dimensional spin lattice with a discretized Hamiltonian consisting of direct exchange, an external field Zeeman term and the weak Dzyaloshinskii-Moriya interaction. In Monte Carlo simulations one can observe the helical, conical and skyrmion phase and, even more interestingly, observe time resolved phase transitions. The goal of this report was to implement such a Monte Carlo code and reproduce results by Buhrandt and Fritz [6], i. e. observe the three different phases and search for phase transitions by repeated sampling at different temperatures and external fields. Furthermore we observe the disappearance of skyrmions both into the fully ordered phase and into the helical phase by dynamically increasing or decreasing the magnetic field respectively as described and observed in [10, 1].

Since most of the limited time designated for this project was spent on the implementation and verification of the Monte Carlo code with simulated annealing and the Metropolis algorithm, we split this work into two parts. The first one provides a general introduction to Monte Carlo methods and describes all algorithmic aspects in great detail. While the lattice model is referred to as a specific example, we do not discuss the physical consequences in detail there. The present complementary report on the other hand describes the results of the simulations without much explanation of the computational methods. Apparently, a theoretic introduction to the lattice model and interactions cannot be absent in any of the two. Therefore, section 1.2 and section 1.3 as well as section 1.4 inevitably have quite some overlap with the introductory sections of the previous report *Sky-MoCa – Introduction to Monte Carlo Methods by Example*.

After this basic introduction, we describe the physical observables and possible diagnostic techniques to analyze the output of the simulations in section 1.5. This concludes our theoretical introduction and we continue in chapter 2 by first sampling the phase space for different temperatures and external fields in section 2.1, where we

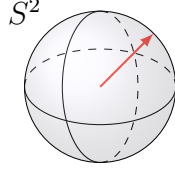


Figure 1.1: We consider three-dimensional spins, i. e. elements of the unit sphere S^2 .

will encounter the helical, conical and skyrmion phase. In section 2.2 we explore the thermodynamic signature of the helimagnetic phase transition by means of the specific heat and susceptibility. Eventually, we discuss the transitions from the skyrmion phase to the helical as well as the totally ordered phase in section 2.3 before we conclude in section 2.4.

1.2 The Spin Lattice Model

A common high-level way to think about magnetism in condensed matter is in terms of complex collective behavior of spins, each of which is associated with a magnetic moment. Astoundingly, this figuratively simple model is quite powerful and allows for a thorough explanation of a wide range of phenomena. Let us consider a three-dimensional lattice with equidistant spacing in each direction. To each lattice site we attach a spin, represented by an element of the unit sphere S^2 , see Figure 1.1. In the following we will often resort to the two-dimensional model for illustration purposes, because it is easier to draw on a two-dimensional surface as illustrated in Figure 1.2. However, all computations solely concern the three-dimensional model. Each vertex of the lattice could for example represent a nucleus in a solid with a rigid crystal like structure. Hence the whole lattice can be interpreted as the regular atomic structure of a simple cubical piece of solid material.

However, we will eventually model chiral magnets like MnSi or $\text{Fe}_{1-x}\text{Co}_x\text{Si}$ which in reality are not well modeled by a homogeneous simple cubic lattice. Therefore, the correspondence between lattice sites and distinguished physical atoms or electrons must not be taken too literally. We will elaborate on this point in section 1.4, when we introduce the continuum model.

We work with a cubic lattice

$$\Sigma := \{1, \dots, N_x\} \times \{1, \dots, N_y\} \times \{1, \dots, N_z\} \subset \mathbb{N}^3 \subset \mathbb{R}^3, \quad (1.1)$$

where we interpret $(i, j, k) \in \Sigma$ as $i\hat{\mathbf{x}} + j\hat{\mathbf{y}} + k\hat{\mathbf{z}} \in \mathbb{R}^3$. Here, $\hat{\mathbf{x}}, \hat{\mathbf{y}}, \hat{\mathbf{z}}$ are the standard basis vectors of \mathbb{R}^3 . Note that we can translate the whole lattice by arbitrary integer linear combinations of the standard basis vectors, thus starting at $(1, 1, 1)$ does not have any physical meaning. It merely corresponds nicely to the numerical implementation in any 1-indexed programming language. At each point $\mathbf{r} \in \Sigma$ we attach a spin $\mathbf{S}_r \in S^2$,

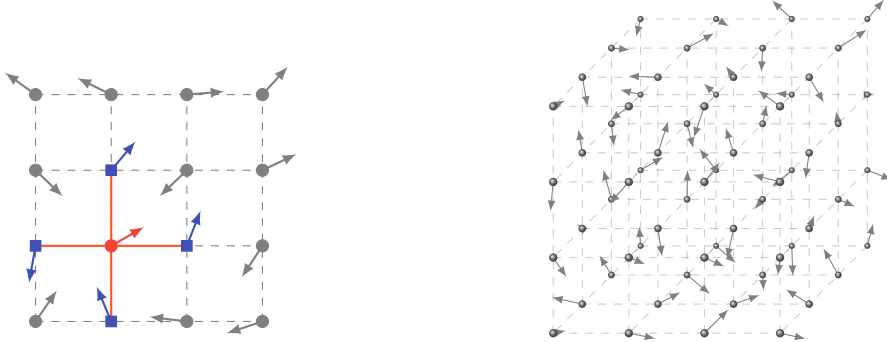


Figure 1.2: On the left side we show a two-dimensional spin lattice. Each lattice site carries a magnetic moment or spin, represented by an arrow of unit length, i.e., in the two-dimensional picture, by an element of S^1 . The neighbors of a lattice site are the ones above, below, left and right in the two-dimensional case. The blue squares are the neighbors of the red circle. The three-dimensional picture on the right side becomes unclear in a two-dimensional drawing rather quickly. Note that the magnetic moments are now also three-dimensional, i.e. elements of the two-dimensional unit sphere S^2 . In three dimensions each vertex has up to six neighbors.

which yields the overall configuration space

$$\Pi := \prod_{\mathbf{r} \in \Sigma} S^2. \quad (1.2)$$

Each element of Π consists of $|\Sigma| = N_x N_y N_z$ spins and thus describes one possible configuration of the whole system. We refer to the specific spin at position $\mathbf{r} \in \Sigma$ by $\mathbf{S}_\mathbf{r} \in S^2$. Note that only the positions of the spins are discretized, but not explicitly their directions. In any real implementation there is always a fine grained discretization caused by the finite number of representable floating point numbers. Discrete vertices and continuous spins mirror nicely the natural crystal structure of solids.

We are going to treat this system thermodynamically by means of the Metropolis algorithm. The macroscopic observables we are particularly interested in are the energy, the magnetization, the specific heat and the susceptibility. While there is a certain similarity to the well known Ising model, there is also a distinct difference. Our model is in the universality class of short ranged interactions, not only in three spatial dimensions, but also with a three-dimensional order parameter, namely the magnetization, with its associated symmetries. At the time of writing, such systems have not been solved analytically, thus it takes great efforts to explore phase transitions and their critical exponents. This is especially true for Monte Carlo simulations, since the correlation length diverges near the critical temperature, which aggravates computing independent samples and results in critical slowing of the simulation. This practical issue will recur in the second chapter.

1.3 Interactions

Ferromagnetic/direct exchange

The most obvious interaction is the *ferromagnetic* or *direct* exchange. Pictorially speaking, it favors constellations where spins that are close to each other point into the same direction. A system only interacting this way will end up in a state where all spins are parallel to each other. The measure for parallelism of two neighboring spins $\mathbf{S}_{\mathbf{r}_1}, \mathbf{S}_{\mathbf{r}_2} \in S^2$ can be expressed as

$$-\mathbf{S}_{\mathbf{r}_1} \cdot \mathbf{S}_{\mathbf{r}_2} = -\|\mathbf{S}_{\mathbf{r}_1}\| \|\mathbf{S}_{\mathbf{r}_2}\| \cos(\alpha), \quad (1.3)$$

where α is the angle between $\mathbf{S}_{\mathbf{r}_1}$ and $\mathbf{S}_{\mathbf{r}_2}$. The minus sign ensures that the energy of two parallel spins is actually smaller than the energy of two perpendicular or even antiparallel ones. While easily comprehensible theoretically, in real materials it is far from obvious whether the direct exchange between localized magnetic moments at different lattice sites is indeed such a prevalent interaction. For many elements like rare earths the unpaired 4f electrons are close to the nucleus and cannot remotely extend out to the orbitals of neighboring atoms. Even for the 3d orbitals of transition metals such as the ferromagnetic Fe, Ni and Co, which extend further from the nucleus, the overlap is barely sufficient to base all magnetic properties on direct exchange. For metals one would have to account for conduction electrons and the band structure of course.

Again this encourages the viewpoint that the lattice Σ does not represent the atomic crystal structure, but is merely a discretized version of a continuous model. In this sense the ferromagnetic exchange can be interpreted as the interaction with a molecular field as in the Weiss theory of ferromagnetism. The mean field character is inherent in the coupling with neighboring spins which correspond to averages of smeared out continuous fields.

While in reality there is almost always a significant portion of indirect exchange involved, our lattice model promotes ferromagnetic interactions to one of the key drivers. It is accounted for by a nearest neighbor interaction only, as shown in Figure 1.2. In the continuum theory, the direct exchange term consists of a gradient, which is a local quantity, i. e. the gradient at a point only depends on an arbitrarily small neighborhood of the point. This corresponds to the *local* or *short ranged* lattice interaction.

Interaction with an external field

Another important and absolutely standard exchange term describes the interaction of the system with an *external magnetic field*. Clearly, every spin tries to align with an external field \mathbf{B} , which we express mathematically via $-\mathbf{B} \cdot \mathbf{S}$ for every spin \mathbf{S} on the lattice. This contribution is also called the *Zeeman energy*. It can be misleading to use terms such as *non-local* or *long ranged* for this exchange, since it is not an interaction between two or more spins within the system, but affects each lattice site independently in the same fashion.

Dzyaloshinskii-Moriya exchange

In this work we are interested in certain crystals that lack inversion symmetry, e.g. MnSi, and thus exhibit chiral magnets. This can emerge as a consequence of the interaction between the excited state of one ion with the ground state of another ion. The excited state would typically arise from spin-orbit interaction of one of the magnetic ions. When the crystal field has an inversion symmetry, this effect will always vanish. Otherwise, for two spins $\mathbf{S}_{\mathbf{r}_1}, \mathbf{S}_{\mathbf{r}_2} \in S^2$ at neighboring positions $\mathbf{r}_1, \mathbf{r}_2 \in \Sigma$ the *Dzyaloshinskii-Moriya* (DM) coupling is proportional to

$$-(\mathbf{S}_{\mathbf{r}_1} \times \mathbf{S}_{\mathbf{r}_2}) \cdot (\mathbf{r}_2 - \mathbf{r}_1). \quad (1.4)$$

Note that $\mathbf{r}_2 - \mathbf{r}_1$ is normalized by definition for neighboring vertices. Since the cross product is zero for parallel vectors and maximal for perpendicular ones, the DM coupling acts against the ferromagnetic interaction and favors constellations where adjacent spins are perpendicular to each other in the plane normal to their connecting line. Typically the DM coupling is weaker than the direct exchange and tends to slightly rotate neighboring magnetic moments with respect to each other. This leads to small angles from one atom to the next and eventually to helical structures, where the spins rotate and trace out a spiral like shape within the material. The DM interaction is also called weak ferromagnetism, since it commonly occurs in antiferromagnetic materials where it adds a small ferromagnetic component.

In the continuum it is described by a term proportional to $-\mathbf{S}(\mathbf{r}) \cdot (\nabla \times \mathbf{S}(\mathbf{r}))$. Just like the gradient, the curl of a vector field is a local property, thus the DM exchange only contributes for adjacent lattice sites.

Ignored interactions

In reality there are always various complex interactions which can never all be captured in a single lattice model. One example is the *dipole-dipole interaction*, which, although rather weak, commonly plays an important role. It will not be part of our model regardless. For two spins $\mathbf{S}_{\mathbf{r}_1}, \mathbf{S}_{\mathbf{r}_2} \in S^2$, it is given by

$$\frac{1}{\|\mathbf{r}\|^3} (\mathbf{S}_{\mathbf{r}_1} \cdot \mathbf{S}_{\mathbf{r}_2} - 3(\mathbf{S}_{\mathbf{r}_1} \cdot \hat{\mathbf{r}})(\mathbf{S}_{\mathbf{r}_2} \cdot \hat{\mathbf{r}})), \quad (1.5)$$

where $\mathbf{r} = \mathbf{r}_2 - \mathbf{r}_1$ and $\hat{\mathbf{r}} = \mathbf{r}/\|\mathbf{r}\|$ points from the location of the first spin in the direction of the second one. The dipole-dipole interaction depends on the distance between the two lattice sites as well as the orientation of the two spins not only relative to each other, but also to the line connecting them. Moreover, the explicit dependence on the relative position already indicates that the dipole-dipole interaction is relevant for each pair of magnetic moments in the system, it is a long ranged interaction. For a lattice with N^3 vertices the number of pairs scales like N^6 . Due to limited computational resources and its relative weakness, most simulations do not take the dipole-dipole exchange into account. We will also disregard it completely in our implementation.

1 Theoretical background

Besides the dipole-dipole interaction we also neglect all other forms of more subtle or long ranged interactions such as superexchange, double exchange or indirect exchange via conduction electrons in metals.

1.4 The Hamiltonian

Let us now combine the FM and DM interaction as well as an external magnetic field to compute the energy for the lattice Σ . To this end we add up the contributions from each spin and for each interaction. This results in the Hamiltonian, i. e. the energy of the system in a given configuration $\pi \in \Pi$

$$H(\pi) = - \sum_{\mathbf{r} \in \Sigma} \left(\mathbf{S}_\mathbf{r} \cdot \mathbf{B} + J \mathbf{S}_\mathbf{r} \cdot (\mathbf{S}_{\mathbf{r}+\hat{\mathbf{x}}} + \mathbf{S}_{\mathbf{r}+\hat{\mathbf{y}}} + \mathbf{S}_{\mathbf{r}+\hat{\mathbf{z}}}) + K (\mathbf{S}_\mathbf{r} \times \mathbf{S}_{\mathbf{r}+\hat{\mathbf{x}}} \cdot \hat{\mathbf{x}} + \mathbf{S}_\mathbf{r} \times \mathbf{S}_{\mathbf{r}+\hat{\mathbf{y}}} \cdot \hat{\mathbf{y}} + \mathbf{S}_\mathbf{r} \times \mathbf{S}_{\mathbf{r}+\hat{\mathbf{z}}} \cdot \hat{\mathbf{z}}) \right), \quad (1.6)$$

which has been proposed in [21] and extended to three dimensions in [6]. Sky-MoCa operates with periodic boundary conditions by default, but one can also open the boundaries in the $\hat{\mathbf{z}}$ direction. We will make use of both options in our simulations. The parameters J , K and \mathbf{B} are sometimes used synonymously for the ferromagnetic, the Dzyaloshinskii-Moriya and the external field interaction terms. The physical behavior of the system strongly depends on these freely adjustable parameters.

The corresponding continuum model is given by [23, 2]

$$H = \int d^3\mathbf{r} \left(\frac{J}{2a} ((\nabla \mathbf{M}_x)^2 + (\nabla \mathbf{M}_y)^2 + (\nabla \mathbf{M}_z)^2) - \frac{1}{a^3} \mathbf{B} \cdot \mathbf{M} + \frac{K}{a^2} \mathbf{M} \cdot (\nabla \times \mathbf{M}) \right). \quad (1.7)$$

This is a commonly used model for chiral magnets that assumes a slow variation in the spin textures, i. e. a certain smoothness in microscopic variations of the magnetization over larger distances. This scale over which spin structures can be considered uniform for all practical purposes is given by the distance a in (1.7).

More accurately, the lattice Hamiltonian in (1.6) should not be viewed as a direct representation of the atomic structure of the material. It is merely a coarse graining or discretization of the continuum model, which itself smears out the fundamentally discrete nature on the level of single atoms to a continuous magnetization field. Therefore, the lattice is more of computational nature which also explains why we do not consider more realistic lattice geometries and do not distinguish different elements. The justification for deriving the lattice model (1.6) from the continuum model (1.7) is given by the so called *construction principle*. It states that the effective low-energy theory derived from the lattice model will only differ from the continuum model by terms that can be neglected in the renormalization-group sense.

Anisotropy

The transition from the continuum theory to a finite homogeneous cubical lattice introduces anisotropies. These anisotropies become apparent in momentum space. The Fourier transform of the direct interaction term of (1.6) reads

$$J \sum_{\mathbf{k}} \alpha_{\mathbf{k}} \mathbf{S}(\mathbf{k}) \cdot \mathbf{S}(-\mathbf{k}), \quad (1.8)$$

where the coefficients $\alpha_{\mathbf{k}}$ are given by

$$\alpha_{\mathbf{k}} = -(\cos(k_x a) + \cos(k_y a) + \cos(k_z a)) = -3 + \frac{a^2}{2} \mathbf{k}^2 + O(k^4). \quad (1.9)$$

The series expansion of the cosine includes arbitrarily high powers of k . In the continuum model (1.7) the ferromagnetic term proportional to $(\nabla \mathbf{M}(\mathbf{r}))^2$ in momentum space only amounts to the square terms in the series expansion. Apparently by discretizing the continuum Hamiltonian we have introduced disruptive higher order anisotropies. For a uniformly ordered state, those anisotropies would not matter, since a uniform state does not feel them. However, for the phases we are interested in, like the skyrmion tubes, they play a crucial role. Thus, we partly compensate those higher order terms by an additive correction to the Hamiltonian given by

$$H'(\pi) = \sum_{\mathbf{r} \in \Sigma} \left(\frac{J}{16} \mathbf{S}_{\mathbf{r}} \cdot (\mathbf{S}_{\mathbf{r}+2\hat{\mathbf{x}}} + \mathbf{S}_{\mathbf{r}+2\hat{\mathbf{y}}} + \mathbf{S}_{\mathbf{r}+2\hat{\mathbf{z}}}) + \frac{K}{8} (\mathbf{S}_{\mathbf{r}} \times \mathbf{S}_{\mathbf{r}+2\hat{\mathbf{x}}} \cdot \hat{\mathbf{x}} + \mathbf{S}_{\mathbf{r}} \times \mathbf{S}_{\mathbf{r}+2\hat{\mathbf{y}}} \cdot \hat{\mathbf{y}} + \mathbf{S}_{\mathbf{r}} \times \mathbf{S}_{\mathbf{r}+2\hat{\mathbf{z}}} \cdot \hat{\mathbf{z}}) \right). \quad (1.10)$$

Buhrandt and Fritz show in [6] that anisotropies indeed hamper the results significantly and that the prefactors $J/16$ and $K/8$ in the next-nearest neighbor interactions are the optimal choice to render higher order deviations from the continuous model as small as possible, while not breaking symmetries of the underlying system. The Hamiltonian used in the simulation is then $H + H'$. Note that H' has the same structure of the FM and DM term of H , but enters with smaller constants and opposite sign. Thus it complements the nearest neighbor exchange by a directly related next-nearest neighbor interaction term. This addition makes a big difference computationally, but is handled analogously to the nearest neighbor interactions, see Figure 1.3.

Although the cubic lattice in principle does feature inversion symmetry and the Hamiltonian (1.6) does not favor any direction at $B = 0$, we find the helical phase in which a certain direction is clearly distinguished even for small external fields. The necessary anisotropies are implicitly generated by discretization errors of our model. After all, a cube is not spherically symmetric, but for example extends further from its center in the diagonal [111] direction than in the [100], [010], or [001] directions.

Fixing the pitch length

Recall that there is a great conflict of interest between the FM and the DM interactions. While the FM term in the Hamiltonian is minimal when all spins are parallel to each

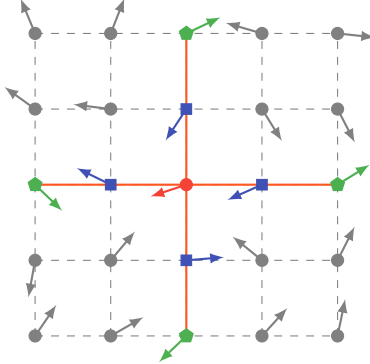


Figure 1.3: We select a spin at position $\mathbf{r} \in \Sigma$ (red circle) and show its nearest neighbors as blue squares and the next-nearest neighbors as green pentagons. Note that although the diagonally adjacent vertices are closer to \mathbf{r} than the next-nearest neighbors, they are not included in any exchange terms of the Hamiltonian.

other, the DM term favors a configuration where neighboring spins are orthogonal. The specific compromise between those effects depends mostly on their respective strengths J and K . In reality the direct interaction J is much stronger and one typically encounters helical or conical structures with long modulation periods for zero or small external fields respectively. For example in MnSi the spins wind around a given modulation axis only once per roughly 40 lattice spacings. By tuning the ratio J/K we can set the periodicity. For a period of N lattice sites, we have to set J/K to $1/\tan(2\pi/N)$. In all our simulations we chose $J = 1$ and $K = \tan(2\pi/10)$, i.e. one full modulation every 10 vertices. Because $K = \tan(2\pi/10) \approx 0.73$ is not much smaller than $J = 1$ we cannot directly model known chiral magnets such as MnSi in our simulation. However, larger periodicities would require much larger grids and thus be computationally infeasible. Moreover, we let the external magnetic field point in the $\hat{\mathbf{z}}$ direction $\mathbf{B} = (0, 0, B)$ and only keep B as a free scalar parameter.

We can fix one of the parameters, in this case J , arbitrarily and then work in abstract lattice units such that everything is implicitly measured in units of J . A computer can only deal with dimensionless numbers and in numerical simulations one often makes convenient, but arbitrary choices. It is sometimes quite difficult to translate the results back to physically meaningful values.

1.4.1 Summary

In this section we have set up our model, which we want to briefly summarize. We work on the lattice

$$\Sigma := \{1, \dots, N_x\} \times \{1, \dots, N_y\} \times \{1, \dots, N_z\} \subset \mathbb{N}^3 \subset \mathbb{R}^3 \quad (1.11)$$

and attach a spin $\mathbf{S}_r \in S^2$ to each lattice site $r \in \Sigma$. This yields the configuration space

$$\Pi := \prod_{r \in \Sigma} S^2. \quad (1.12)$$

On Π we define the Hamiltonian $H + H'$ from (1.6) and (1.10) where we implement periodic or partially open boundary conditions. The parameters $J = 1$ and $K = \tan(2\pi/10)$ of the FM and DM interaction are fixed, which leaves us only with the magnetic field in the $\hat{\mathbf{z}}$ direction B and the temperature T of the simulated annealing algorithm as free scalar parameters.

1.5 Observables and Analysis

As expounded in great detail in the accompanying report on Monte Carlo methods, in the simplest case, we compute N independent samples of the equilibrated system at a fixed temperature T and magnetic field B according to the Boltzmann distribution. Observables are given by the averages over those configurations and errors are computed via the jackknife estimator.

At high temperatures and away from phase transitions this reliably yields precisely the phases one would expect from experiments and previous independent simulations. Naturally, at low temperatures or close to critical points two potential problems emerge. First, as correlation lengths diverge it becomes increasingly computationally expensive to equilibrate the system and obtain independent samples, which in turn spoils error estimates.

Second, starting at low temperatures facilitates the danger of getting stuck in a certain region of the phase space not sampling the energetically favorable phase. As suggested earlier [6] one way to prevent this issue is to slowly approach the target temperature and magnetic field in various ways. The run with the lowest energy $\langle E \rangle$ is chosen as the true physical minimum. There are uncountably many ways to reach the target temperature and external field. However, it always makes sense to start at high temperature to allow the system to sample every part of the phase space with a reasonably high probability. Moreover, thermalization times and correlation lengths are short at high temperatures. Plausible simulated annealing schedules to reach the target temperature T^* and magnetic field B^* are therefore

- Start at a high temperature T_0 and with the target magnetic field B^* . Then slowly cool the system to the target temperature T .
- Slowly cool from a high temperature T_0 to the target temperature T^* at a large magnetic field B_0 . Then slowly decrease the magnetic field to the target field B^* .
- Slowly cool from a high temperature T_0 to the target temperature T^* at zero magnetic field $B_0 = 0$. Then slowly increase the magnetic field to the target field B^* .

1 Theoretical background

Ideally, one would compute all three scenarios in parallel. In case they all agree one would confidently declare the result to be the thermodynamic state. In case of disagreement the run which results in the lowest energy is our best shot at the true physical state. Note that even with advanced parallel tempering Monte Carlo simulations the Metropolis algorithm sometimes gets trapped in a metastable state. In our implementation we did not use parallel tempering nor did we have the computational resources and time to compare different annealing schedules. Fortunately, we could nevertheless identify all three phases. On the downside it was impossible to draw precise boundaries and we had problems with both metastable traps and diverging correlation lengths at low temperatures.

Besides the energy E from $H + H'$ and the magnetization

$$\mathbf{M} := \frac{1}{|\Sigma|} \sum_{\mathbf{r} \in \Sigma} \mathbf{S}_{\mathbf{r}} \quad (1.13)$$

we are also interested in the specific heat and the magnetic susceptibility in the $\hat{\mathbf{z}}$ direction given by

$$c_V(T) = \frac{\langle E^2 \rangle - \langle E \rangle^2}{|\Sigma| T^2} \quad \text{and} \quad \chi_{zz}(T) = \frac{\langle M_z^2 \rangle - \langle M_z \rangle^2}{|\Sigma| T} \quad (1.14)$$

respectively. Those will prove particularly helpful in detecting phase transitions during the analysis of the results in chapter 2.

The canonic way to distinguish different thermodynamic phases of the system is to plot the whole spin structure, i. e. a three-dimensional lattice with a vector attached to each vertex. However, this is somewhat flawed, because visualization possibilities on a two-dimensional screen are limited such that the classification becomes highly subjective and ambiguous. Recalling that we expect to find periodic excitations in each phase, we might be able to get a better grip on the task in reciprocal space. Thus we first compute the discrete Fourier transform

$$\langle \mathbf{S}_{\mathbf{k}} \rangle = \frac{1}{N} \sum_{\mathbf{r}} \langle \mathbf{S}_{\mathbf{r}} \rangle e^{-i \mathbf{k} \cdot \mathbf{r}}. \quad (1.15)$$

componentwise, where $\langle \mathbf{S}_{\mathbf{r}} \rangle$ is already a thermal average of the spin at the vertex $\mathbf{r} \in \Sigma$ over several configurations in the Markov chain. The Bragg intensity profile is then proportional to the squared norm of $\langle \mathbf{S}_{\mathbf{k}} \rangle$,

$$\mathbf{I}(\mathbf{k}) \propto \| \langle \mathbf{S}_{\mathbf{k}} \rangle \|^2. \quad (1.16)$$

Now we have already reduced the problem from classifying a three-dimensional vector field in three dimension to a scalar field in three dimensions. Everything beyond two dimensions is still rather inconvenient to handle visually. If we further project the Bragg intensity to various coordinate planes via

$$I_{xy}(i, j) := \sum_{k=1}^{N_z} \langle \mathbf{S}_{(i,j,k)} \rangle \quad \text{and} \quad I_{xz}(i, k) := \sum_{j=1}^{N_y} \langle \mathbf{S}_{(i,j,k)} \rangle, \quad (1.17)$$

1.5 Observables and Analysis

we end up with scalar functions in two dimensions, which can nicely be displayed as grayscale images.

Moreover, due to the order in the helical, conical and skyrmion phase, those images will feature only few bright spots in different patterns, which allows a convenient classification. In Figure 2.1 we show the characteristic projected Bragg intensity patterns for the helical, conical and skyrmion phase. A detailed discussion of these images follows in section 2.1. Now we are equipped with the theoretic foundation to look at some results of the simulations.

2 Results

In this chapter we present some results from simulations performed with *Sky-MoCa*, a Monte Carlo code written in Julia [4], publicly available at <https://github.com/nikikilbertus/Sky-MoCa>.

2.1 Thermodynamic Phases

One of the main goals of this project was to explore the phase space by Monte Carlo simulations at different target temperatures T and external fields B . First, let us describe the three phases by reference to Figure 2.1. The temperature and magnetic field for each of these simulations is shown in Figure 2.2.

In the top left area we illustrate the helical phase. The spins wind around the easy axis, which in our simulation is in the [111] direction. If we contracted them along the easy axis they would all lie in a plane, hence are perpendicular to the pitch axis. We also show the Bragg intensity (1.17) projected to the xz (top) and xy (bottom) planes. We see two distinct maxima since the helix winds diagonally through the cube. In all images of the Bragg intensity we have subtracted the mean of the original field first to discard the constant offset.

On the right side we illustrate the conical phase, where the rotation axis points in the \hat{z} axis parallel to the magnetic field. Thus the spins are not perpendicular to the axis, but have a constant component in the \hat{z} direction. If we contracted them along the \hat{z} axis, they would form a cone, which is where the phase got its name from. Due to the alignment with the external field the Bragg intensity projection to the xy plane is now a single dot. It represents the single distinct winding mode of the spins.

In the bottom region we show the skyrmion phase. One can clearly see the tubes parallel to the magnetic field throughout the simulation volume and their hexagonal order. This is also clearly visible as the characteristic hexagon in the Bragg intensity projection to the xy plane. The red arrows point in the direction of the magnetic field, i.e. along the \hat{z} direction. At the skyrmion tubes they rotate into the xy plane in a circular fashion until their z component vanishes roughly between the yellow and green arrows. Inside the circle the spins rotate further down until they are antiparallel to the magnetic field (blue arrows), i.e. they point in the $-\hat{z}$ direction.

2 Results

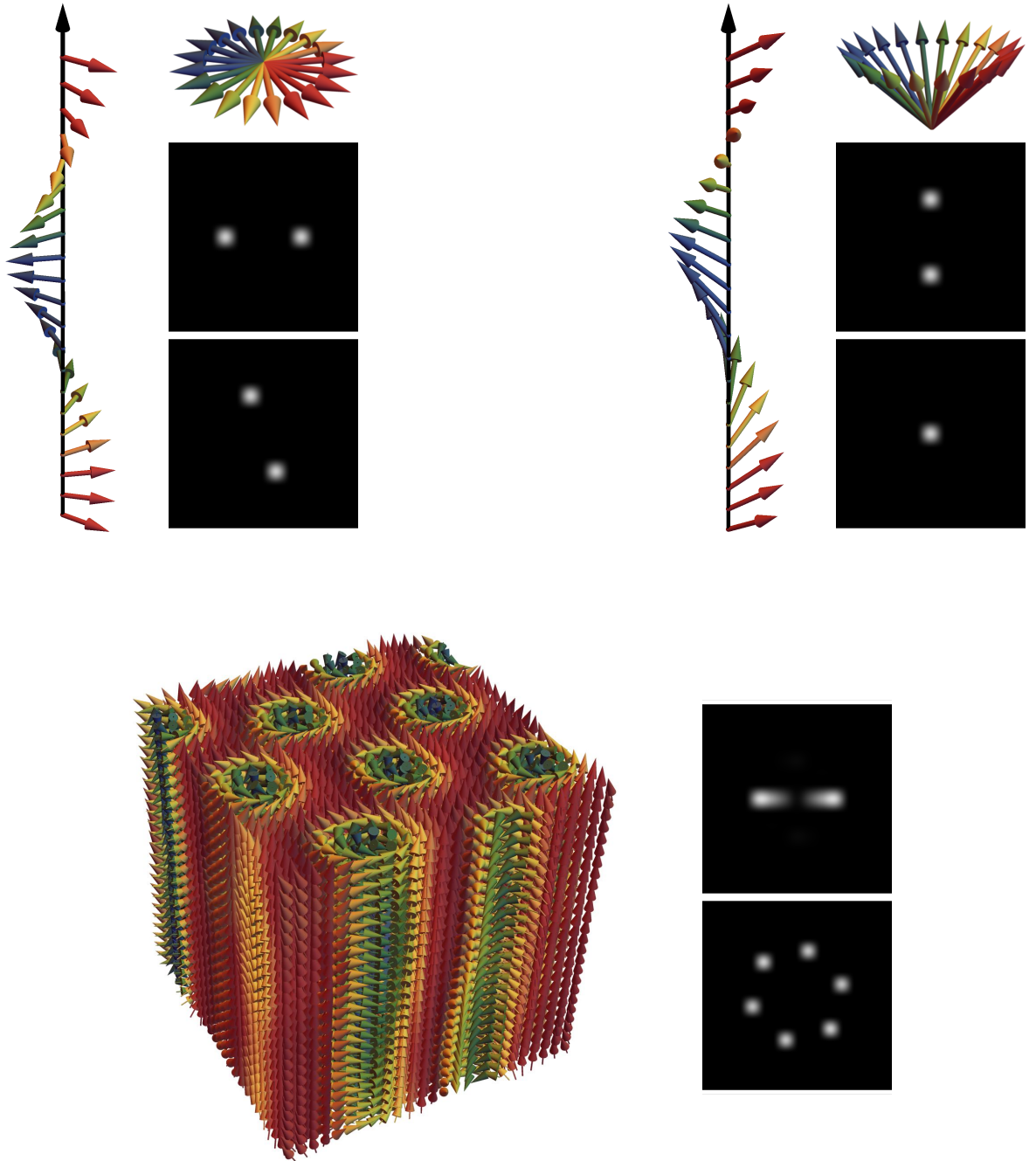


Figure 2.1: We illustrate the helical (top left), conical (top right) and skyrmion (bottom) phases. The Bragg intensity projections (1.17) are given for the xz (top) and xy (bottom) plane respectively. A detailed description can be found in the text.

As we have already mentioned in section 1.5, we could not perform various annealing schedules to reach the true physical state for the whole parameter range. Therefore we adopted the phase diagram in Figure 2.2 from Buhrandt and Fritz [6]. We marked the

positions where we recorded the data for Figure 2.1. These runs were done on a 30^3 lattice with periodic boundary conditions using 2000 configurations separated by just 30 lattice sweeps each. The number of lattice sweeps should be significantly higher particularly for smaller temperatures to yield truly uncorrelated samples. A detailed explanation can be found in the accompanying report *Sky-MoCa – Introduction to Monte Carlo Methods by Example*. However, a tradeoff between computation time and error estimates had to be made. In the following all error bars have been computed by the jackknife method and should be taken with a grain of salt.

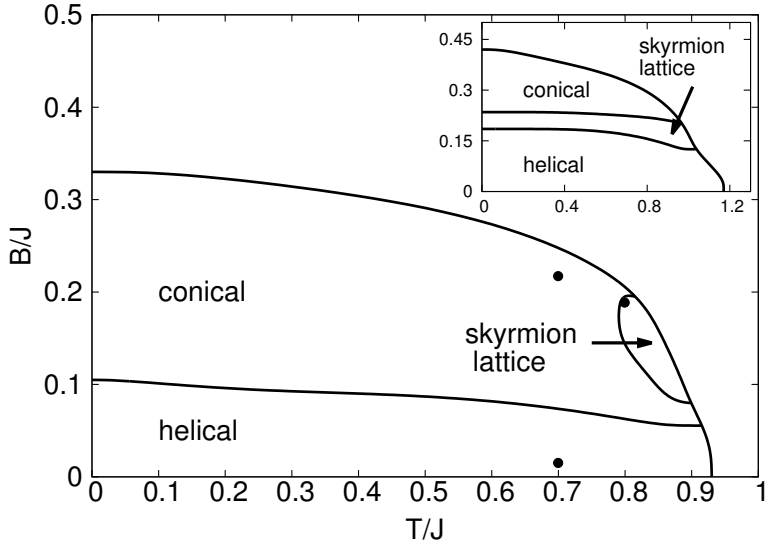


Figure 2.2: The phase diagram of the skyrmion phase as shown by Buhrandt and Fritz in [6]. The inset is the phase diagram one obtains without the counter terms in H' to suppress unwanted anisotropy effects. The three circles indicate the points in phase space we have used for the Bragg intensity projections in Figure 2.1.

Instead of densely sampling the whole phase space, we decided to only look at some specific transitions. The first one is the transition from the high temperature regime $T/J > 1$ into the low temperature regime $T/J < 0.5$ for different magnetic fields.

2.2 The Helimagnetic Phase Transition

The theory of the temperature driven phase transition at high external fields has first been described by Brazovskii [5] and has been investigated extensively experimentally [8, 18, 14, 19, 3, 9]. In the simulation we perform simulated annealing starting at a high temperature $T/J = 3$ down to $T/J = 0$ at various fixed magnetic fields. While slowly decreasing the temperature we take 1000 configurations at each step. The configurations are separated by 30 lattice sweeps. Figure 2.3 shows the resulting

2 Results

behavior of the heat capacity. There are distinct spikes at low external fields around a critical temperature of $T_c \approx 0.9J$. This phenomenon can be verified by looking at the susceptibility for $B = 0$, see Figure 2.4.

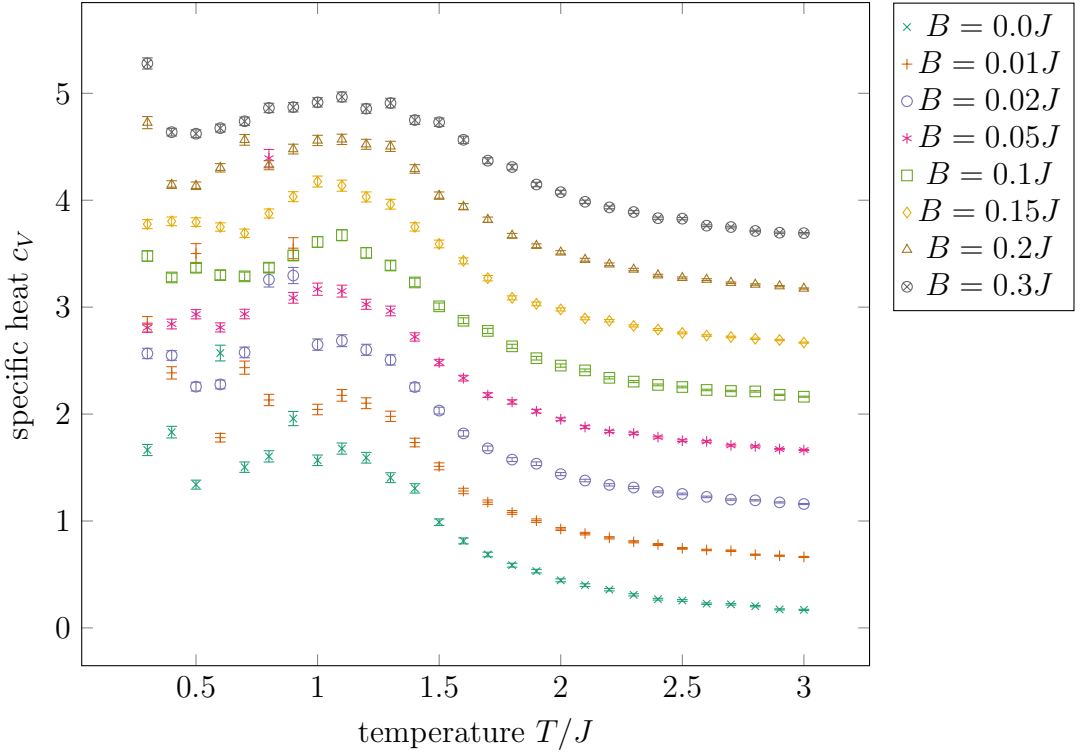


Figure 2.3: We plot the specific heat as a function of temperature for various external fields. The different plots have been offset by 0.5 each for better visibility. Thus they all roughly converge to 1 for $T \rightarrow 0$. Besides the broad maximum they all exhibit corresponding to the Schottky anomaly, at low magnetic fields there is a highly localized and distinct spike around $T \approx 0.9J$. As a discontinuity in the heat capacity, this hints towards a phase transition. The errors are computed with the jackknife method with 1000 configurations each.

2.3 Unwinding Skyrmions

Let us now start in the skyrmion phase and decrease or increase the magnetic field to investigate the transitions to the helical and fully ordered phase. To this extent we follow the description in the supplemental material of [10] and first anneal at constant magnetic field $B/J = 0.16$ from $T/J = 1.5$ to $T/J = 0.7$. Due to the topological stability of the skyrmion tubes they survive after their formation at roughly $T/J = 0.9 - 0.8$ all the way down to $T = 0$. Hence when we arrive at $T/J = 0.7$ the system

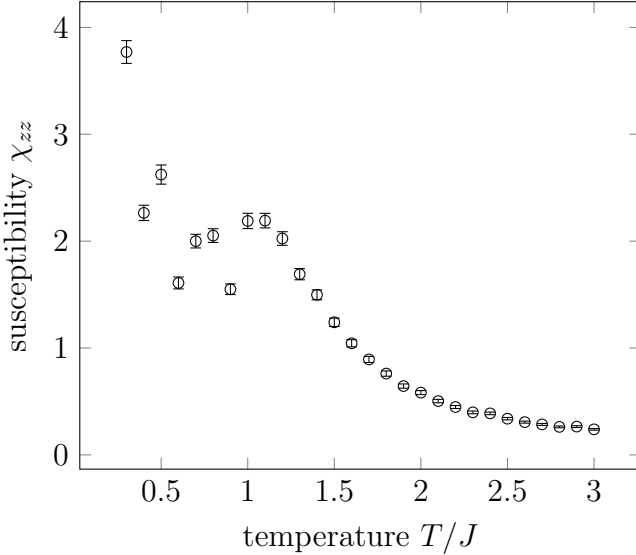


Figure 2.4: The critical behavior around $T_c \approx 0.9J$ is clearly visible in the temperature dependent susceptibility at zero magnetic field.

is in a stable skyrmion phase as shown in Figure 2.5. At this stage the whole system looks something like the one shown in Figure 2.1.

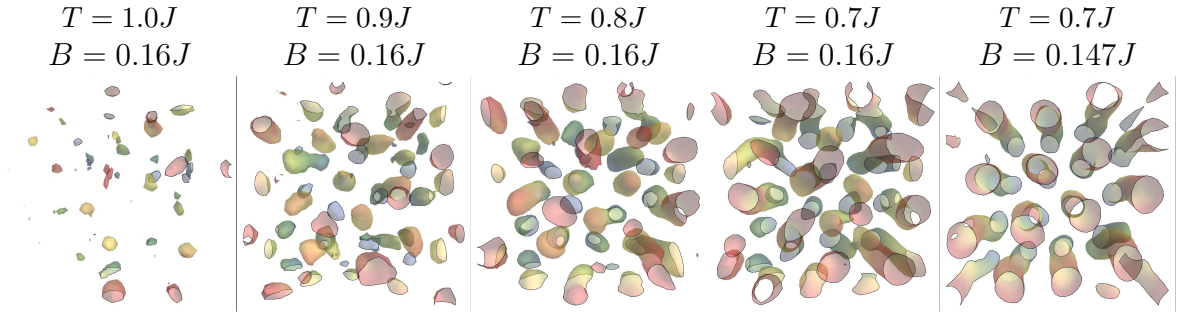


Figure 2.5: We show a top view, i. e. looking in the $-\hat{z}$ direction, of the system at some snapshots during the annealing phase from $T/J = 1.5$ to $T/J = 0.7$. The shaded surfaces are contours of vanishing z component of the spins. This corresponds to the yellow to green transition of the arrows in Figure 2.1 and can be interpreted as the boundaries of the skyrmion tubes. The skyrmion tubes build up and stabilize further after reaching the target temperature.

Subsequently we decrease the magnetic field from $B/J = 0.16$ in steps of 0.0005 all the way down to $B/J = 0.0005$. At smaller magnetic fields the radius of the skyrmion tubes increases and they become increasingly unstable, which is expressed in a sort of wobbling. Once two tubes come in contact, a topological defect, which can be interpreted as a magnetic monopole and is thus often called *hedgehog*, moves

2 Results

along the tubes and zips them together. Again we show some selected snapshots of the dynamics in Figure 2.6. The first contact between tubes has already been established at $B = 0.054J$, but the skyrmions have separated again. The whole phase transition occurs between $B = 0.04J$, where all tubes are still well separated and $B = 0.03$, where all tubes have connected to form wavy sheets characteristic for the helical phase. This value is slightly smaller than what we would infer from the phase diagram in Figure 2.2. However, for some degree of temporal resolution the external field schedule advances rather fast so that we might not give the system enough time to transition at higher magnetic fields.

Due to the rapid dynamics of the transition from the skyrmion phase to the helical phase, we cannot average over too many configurations. If the thermal average contains a large number of samples, the dynamic effects will be averaged out completely and we could not resolve the transition temporally. However, a certain number of configurations is needed for reasonable statistics. We chose to discard the first 250 lattice sweeps after each change in the magnetic field and then record 250 configurations separated by 30 lattice sweeps.

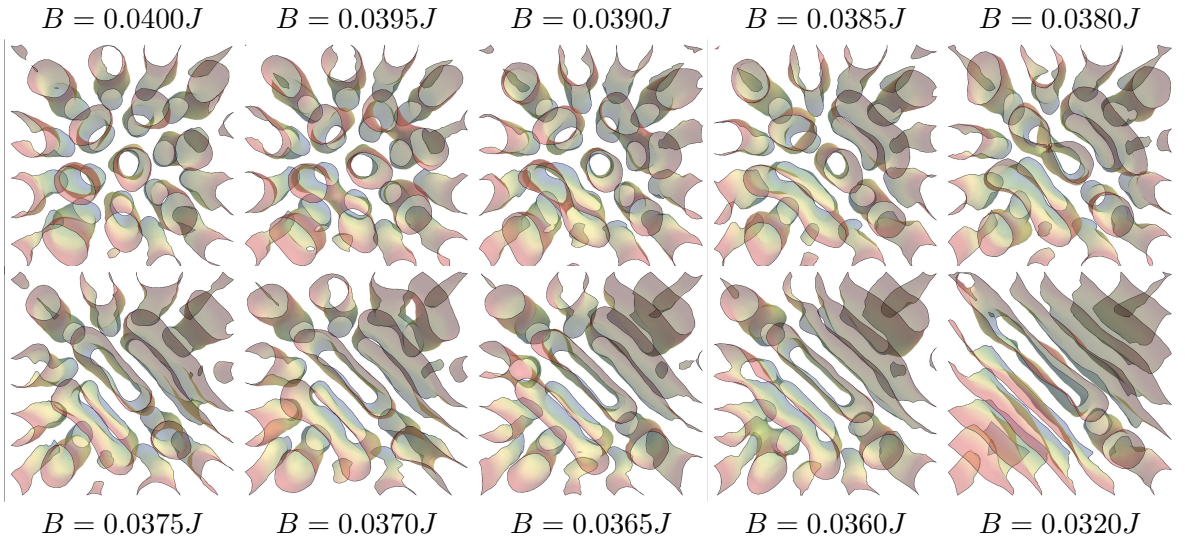


Figure 2.6: Again, we show a top view, i.e. looking in the $-\hat{z}$ direction, of the system at some snapshots when decreasing the external magnetic field. All images have been taken at $T = 0.7J$. Note that the last snapshot is significantly later than the others. The configuration of the second to last one does not change much for quite some time.

Note that we have to open the boundaries in the \hat{z} direction for this simulation. With periodic boundary conditions in all directions, the tubes could not come into contact at the bottom of the cube, while staying intact on the top surface for instance. The dimensions of the simulation lattice are $42 \times 42 \times 30$ with 30 points along the \hat{z} axis.

In the second part of this section we increase the magnetic field. We use the same setup and start after the temperature annealing at $T = 0.7J$ and $B = 0.16J$ to increase the magnetic field in steps of 0.002. The skyrmion tubes slowly shrink in radius and become very well separated before they start to disappear, see Figure 2.7. This is in accordance with experiment [1]. Starting from $B \approx 0.21J$ all tubes have vanished by the time $B \approx 0.27J$.

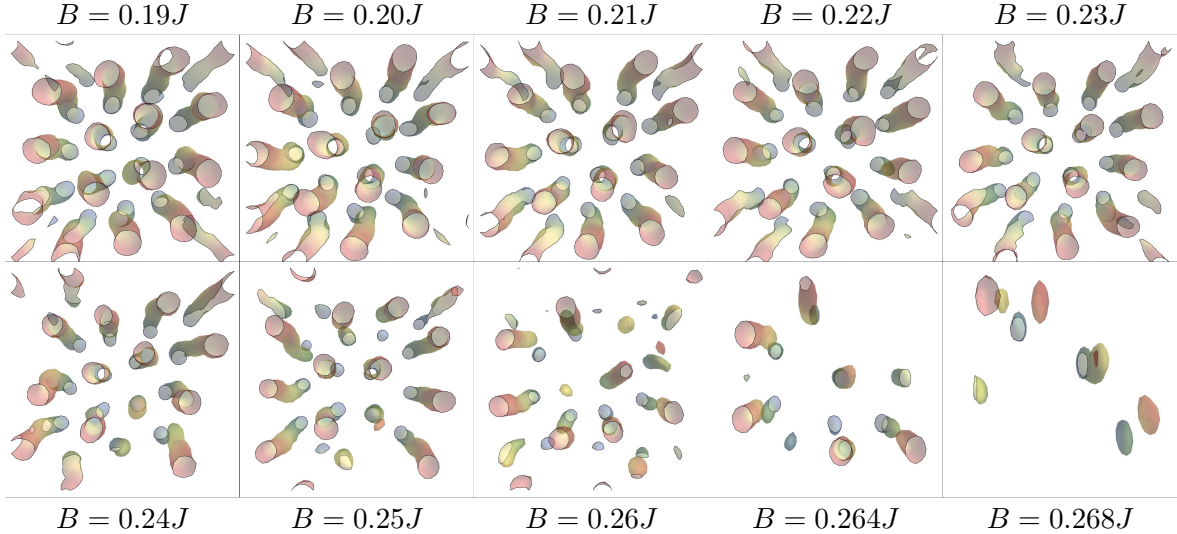


Figure 2.7: Again, we show a top view, i. e. looking in the $-\hat{\mathbf{z}}$ direction, of the system at some snapshots when decreasing the external magnetic field. All images have been taken at $T = 0.7J$.

2.4 Conclusion

We have shown that fully non-perturbative classical three-dimensional Monte Carlo lattice simulations are a valuable tool to investigate chiral magnets and the skyrmion phase. Furthermore we demonstrated that the implementation of the simulated annealing algorithm, at least a simple version of it, is rather straight forward and still yields interesting results. With a more sophisticated parallel tempering Monte Carlo code and sufficient computational resources the whole phase diagram can be reproduced. Thermodynamic properties in the temperature driven helimagnetic phase transition match experimental data well. The isothermal transitions from the skyrmion phase into the helical and the magnetically ordered phase are qualitatively consistent with experiments.

References

- [1] C. Back et al., *TBA*, to appear on the arxiv.
- [2] P Bak and M H Jensen, *Theory of helical magnetic structures and phase transitions in mnsi and fege*, Journal of Physics C: Solid State Physics **13** (1980), no. 31, L881.
- [3] A. Bauer, M. Garst, and C. Pfleiderer, *Specific heat of the skyrmion lattice phase and field-induced tricritical point in mnsi*, Phys. Rev. Lett. **110** (2013), 177207.
- [4] Jeff Bezanson, Alan Edelman, Stefan Karpinski, and Viral B. Shah, *Julia: A fresh approach to numerical computing*, (2014).
- [5] SA Brazovskii, *Phase transition of an isotropic system to a nonuniform state*, Soviet Journal of Experimental and Theoretical Physics **41** (1975), 85.
- [6] S. Buhrandt and L. Fritz, *Skyrmion lattice phase in three-dimensional chiral magnets from Monte Carlo simulations*, Phys. Rev. B **88** (2013), no. 19, 195137.
- [7] C. Heo, N. S. Kiselev, A. K. Nandy, S. Blügel, and T. Rasing, *Switching of chiral magnetic skyrmions by picosecond magnetic field pulses via transient topological states*, Scientific Reports **6** (2016), 27146.
- [8] M. Janoschek, M. Garst, A. Bauer, P. Krautscheid, R. Georgii, P. Böni, and C. Pfleiderer, *Fluctuation-induced first-order phase transition in dzyaloshinskii-moriya helimagnets*, Phys. Rev. B **87** (2013), 134407.
- [9] D. Lamago, R. Georgii, and P. Böni, *Magnetic susceptibility and specific heat of the itinerant ferromagnet mnsi*, Physica B: Condensed Matter **359–361** (2005), 1171 – 1173, Proceedings of the International Conference on Strongly Correlated Electron Systems.
- [10] P. Milde, D. Köhler, J. Seidel, L. M. Eng, A. Bauer, A. Chacon, J. Kindervater, S. Mühlbauer, C. Pfleiderer, S. Buhrandt, C. Schütte, and A. Rosch, *Unwinding of a skyrmion lattice by magnetic monopoles*, Science **340** (2013), no. 6136, 1076–1080.
- [11] S. Mühlbauer, B. Binz, F. Jonietz, C. Pfleiderer, A. Rosch, A. Neubauer, R. Georgii, and P. Böni, *Skyrmion lattice in a chiral magnet*, Science **323** (2009), no. 5916, 915–919.

References

- [12] W. Münzer, A. Neubauer, T. Adams, S. Mühlbauer, C. Franz, F. Jonietz, R. Georgii, P. Böni, B. Pedersen, M. Schmidt, A. Rosch, and C. Pfleiderer, *Skyrmion lattice in the doped semiconductor $fe_{1-x}co_xSi$* , Phys. Rev. B **81** (2010), 041203.
- [13] Naoto Nagaosa and Yoshinori Tokura, *Topological properties and dynamics of magnetic skyrmions*, Nat Nano **8** (2013), no. 12, 899–911, Review.
- [14] C. Pfleiderer, *Experimental studies of weakly magnetic transition metal compounds*, Journal of Magnetism and Magnetic Materials **226–230, Part 1** (2001), 23 – 29, Proceedings of the International Conference on Magnetism (ICM 2000).
- [15] C Pfleiderer, T Adams, A Bauer, W Biberacher, B Binz, F Birkelbach, P Böni, C Franz, R Georgii, M Janoschek, F Jonietz, T Keller, R Ritz, S Mühlbauer, W Münzer, A Neubauer, B Pedersen, and A Rosch, *Skyrmion lattices in metallic and semiconducting $b20$ transition metal compounds*, Journal of Physics: Condensed Matter **22** (2010), no. 16, 164207.
- [16] Jan Seidel, *Topological structures in ferroic materials*, Springer, 2016.
- [17] S. Seki, X. Z. Yu, S. Ishiwata, and Y. Tokura, *Observation of skyrmions in a multiferroic material*, Science **336** (2012), no. 6078, 198–201.
- [18] S. M. Stishov, A. E. Petrova, S. Khasanov, G. Kh. Panova, A. A. Shikov, J. C. Lashley, D. Wu, and T. A. Lograsso, *Magnetic phase transition in the itinerant helimagnet MnSi: Thermodynamic and transport properties*, Phys. Rev. B **76** (2007), 052405.
- [19] S M Stishov, A E Petrova, S Khasanov, G Kh Panova, A A Shikov, J C Lashley, D Wu, and T A Lograsso, *Heat capacity and thermal expansion of the itinerant helimagnet mnsi*, Journal of Physics: Condensed Matter **20** (2008), no. 23, 235222.
- [20] Y. Tokunaga, X. Z. Yu, J. S. White, H. M. Ronnow, D. Morikawa, Y. Taguchi, and Y. Tokura, *A new class of chiral materials hosting magnetic skyrmions beyond room temperature*, Nat Commun **6** (2015), Article.
- [21] Su Do Yi, Shigeki Onoda, Naoto Nagaosa, and Jung Hoon Han, *Skyrmions and anomalous hall effect in a dzyaloshinskii-moriya spiral magnet*, Phys. Rev. B **80** (2009), 054416.
- [22] X. Z. Yu, N. Kanazawa, Y. Onose, K. Kimoto, W. Z. Zhang, S. Ishiwata, Y. Matsui, and Y. Tokura, *Near room-temperature formation of a skyrmion crystal in thin-films of the helimagnet fege*, Nat Mater **10** (2011), no. 2, 106–109.
- [23] X. Z. Yu, Y. Onose, N. Kanazawa, J. H. Park, J. H. Han, Y. Matsui, N. Nagaosa, and Y. Tokura, *Real-space observation of a two-dimensional skyrmion crystal*, Nature **465** (2010), no. 7300, 901–904.